RESEARCH ARTICLE
PLANETARY SCIENCES

Earth and Planetary Physics
9: 1125–1134, 2025
doi: 10.26464/epp2025078

The fitting of a dipolar magnetic field by a dipole model

ZhaoJin Rong[1,2,3*], Yong Wei[1,2], Fei He[1,2], Lucy Klinger[4,5], YanYan Yang[6], JiaWei Gao[1,2], Zhen Shi[1,2], HuaPei Wang[7], ShuHui Cai[2,8], HuaFeng Qin[2,8], and RiXiang Zhu[2,8]

[1]Key Laboratory of Planetary Science and Frontier Technology, Institute of Geology and Geophysics, Chinese Academy of Sciences, Beijing 100029, China;

[2]College of Earth and Planetary Sciences, University of Chinese Academy of Sciences, Beijing 100083, China;

[3]Mohe Observatory of Geophysics, Institute of Geology and Geophysics, Chinese Academy of Sciences, Beijing 100029, China;

[4]The Shanghai Institute for Mathematics and Interdisciplinary Sciences, Shanghai 200433, China;

[5]Fudan University, Shanghai 200433, China;

[6]National Institute of Natural Hazards, Ministry of Emergency Management of China, Beijing 100085, China;

[7]Paleomagnetism and Planetary Magnetism Laboratory, School of Geophysics and Geomatics, China University of Geosciences, Wuhan 430074, China;

[8]State Key Laboratory of Lithospheric Evolution, Institute of Geology and Geophysics, Chinese Academy of Sciences, Beijing 100029, China

Key Points:

- A technique based on a single dipole model is used to invert the dipolar magnetic field.
- This technique can successively separate and invert the multiple parameters of the model.
- Applications of the technique demonstrate its robustness, and it can be applied widely in the fields of geomagnetism and planetary magnetism.

Citation: Rong, Z. J., Wei, Y., He, F., Klinger, L., Yang, Y. Y., Gao, J. W., Shi, Z., Wang, H. P., Cai, S. H., ... Zhu, R. X. (2025). The fitting of a dipolar magnetic field by a dipole model. *Earth Planet. Phys.*, *9*(6), 1125–1134. http://doi.org/10.26464/epp2025078

Abstract: Many planets, including the Earth, possess a global dipolar magnetic field. To diagnose the interior source of the dipolar field, researchers usually adopt a dipole model consisting of six parameters to fit the observed dataset of the magnetic field. However, the simultaneous fitting of these parameters often leads to multiple local optimal parameter sets. To address this fitting dilemma, Rong ZJ et al. (2021) recently developed a current loop model. This technique can successively separate and invert the loop parameters. Here, we further show how this technique can be reduced and modified to fit a dipole model. Applications of this reduced technique to the International Geomagnetic Reference Field model and the Martian crustal field model highlight its unique ability to diagnose both the planetary global dipolar field and the local crustal field anomaly, a capability that sets it apart from existing methods. The potential impact of this technique on geomagnetism and planetary magnetism is significant, given its unique ability to diagnose both the planetary global dipolar field and the local crustal field anomaly.

Keywords: geomagnetic field; magnetic dipole; inversion; dipolar magnetic field; magnetic anomaly; crustal magnetic field; magnetic sources; eccentric dipole

---

Plain Language Summary

The source of any dipolar magnetic field can be approximated by a magnetic dipole to the first order. The traditional least-squares methods used to invert a dipole model inevitably involve the simultaneous fitting of multiple parameters of the dipole model, which can result in multiple local optimal parameter sets. In contrast, the method we present here can successively separate and invert the dipole parameters. Applications to the International Geomagnetic Reference Field model and the Martian crustal field model demonstrate that the parameters inverted by our technique are reasonable; thus, this technique can be applied widely in the fields of geomagnetism and planetary magnetism.

1. Introduction

Most planets in our solar system possess a global dipolar magnetic field. The standard or traditional way to study the planetary magnetic field is to perform a spherical harmonic analysis (SHA), which treats the measured magnetic field as the sum of associated Legendre polynomials (Chapman and Bartels, 1940; Merrill et al., 1996). The coefficients of these associated Legendre polynomials, referred to as Gauss coefficients, can be determined based on the sampled dataset of the magnetic field. The planet-centered dipole component is defined by the first three coefficients of the internal field, whereas the other coefficients of the internal field can represent the different multipole (quadrupole, octupole, etc.) components. To make the approximation of the dipole model more reasonable, an eccentric dipole approximation is also made by using the first eight internal Gauss coefficients, where

---

Correspondence to: Z. J. Rong, rongzhaojin@mail.iggcas.ac.cn
Received 17 MAR 2025; Accepted 04 JUN 2025.

the eccentric dipole has the same dipole moment and axis orientation as the original geocentered dipole (e.g., Fraser-Smith, 1987). However, Sano (1991) and Sano and Sugiura (1992) found that if all Gauss coefficients are considered, the moment and location of a fitted eccentric dipole are different from those obtained by the classical method of using the first eight internal Gauss coefficients. In other words, a real eccentric dipole will be mathematically expanded as a planet-centered dipole plus a series of higher multipole fields in terms of the SHA (Merrill et al., 1996). Thus, when addressing the source of the dipolar field, one may have to consider a source model, such as dipoles or current loops (note that the dipole is a special case of the current loop when the loop radius is zero), to fit the observed field dataset directly.

In earlier stages, many geomagnetism researchers indeed alternatively tried to fit the *in situ* measurements of the magnetic field directly, based on the models of one or multiple magnetic dipoles or current loops (e.g., Alldredge and Hurwitz, 1964; Alldredge and Stearns, 1969; Peddie, 1979; Demina and Farafonova, 2016; Rong ZJ et al., 2021 and references therein). The dipole model has also been used to fit a spacecraft's magnetic field measurements of Mercury (Ness et al., 1974) and Jupiter (Smith et al., 1976). The main challenge of fitting algorithms in these models is that the simultaneous least-squares fitting of model parameters requires the initial input of parameters, which results in multiple local solutions. Thus, Peddie (1979) argued that no general technique exists for finding the best solution in the parameter space, even for a single loop or dipole model.

In contrast to the traditional least-squares fitting, a recent technique developed by Rong ZJ et al. (2021) based on a single circular loop model can effectively separate the multiple parameters of the model and successively invert these parameters. In other words, the inversion technique of Rong ZJ et al. (2021) can avoid the dilemma of simultaneous fitting of multiple parameters to find the best solution. The model tests and applications showed the validity and robustness of this technique. Moreover, this technique can offer several error indicators when evaluating how much the sampled dataset deviated from the fitted loop model. (A comparison with the traditional least-squares fitting is provided in the Supporting Information of Rong ZJ et al., 2021.)

Although the loop technique presented by Rong ZJ et al. (2021) works well, several issues must be considered when simplifying the loop model into a dipole model:

(1) The applications by Rong ZJ et al. (2021) showed that the loop technique would fail in some cases, such as in the case of fitting an ideal dipole field because the optimal radius of the loop model is supposed to be zero in this case, and the optimal fitting by computer would be forced to end when the trial radius becomes negative. In other words, the optimal loop radius cannot always be found numerically.

(2) The analytic formula for the magnetic field generated by the loop model is more complicated than that of the dipole field. In most cases, researchers would rather choose a simple dipole model to describe the dipolar field.

(3) Given that any magnetic source can be seen as a dipole in first-order approximation, the inversion technique of a dipole model is essential in diagnosing the magnetic source generally.

Thus, to address the inversion of the dipolar field in general, here we show how the loop technique by Rong ZJ et al. (2021) can be modified to fit a dipole model even though the inversion algorithms for the two models are nearly the same. With this technique, the six parameters of the dipole (three for the dipole center, two for the axis orientation, and one for the dipole moment) can be separated and inverted robustly.

The structure of this paper is organized as follows. Section 2 introduces the modified technique to fit the dipole model. Section 3 shows its application to a sampled dataset from the International Geomagnetic Reference Field (IGRF) model, as well as its application to selected regions of the Martian crustal field model. Finally, we offer a discussion in Section 4 and conclusions in Section 5.

2. Methodology

Utilizing a spacecraft's sampled dataset of magnetic field vectors, Rong ZJ et al. (2021) presented a technique to fit the global geomagnetic field based on a single circular current loop model. This loop technique can be reduced to fit an eccentric dipole model (in which case the loop radius is zero). In this section, with the assumption of the interior source of a dipole, we describe how the technique by Rong ZJ et al. (2021) can be modified to invert the dipole parameters.

2.1 Coordinate Systems

Because the intrinsic magnetic field of the planet is corotating with the planet's rotation, it is convenient to address this technique in the planetocentric coordinate that is fixed with the planet's rotation. In this coordinate, the origin point is at the center of the planet, the *x*-axis points toward the intersection of the equator and the primary meridian (e.g., the Greenwich meridian for the Earth), the *z*-axis is parallel to the planet's axis of rotation (positive to the north), and the *y*-axis completes a right-handed orthogonal set.

In the planetocentric coordinates *xyz*, as shown in Figure 1, the magnetic field is assumed to be induced by a magnetic dipole. The dipole center is at $\boldsymbol{r}_0\,(x_0\hat{\boldsymbol{x}}, y_0\hat{\boldsymbol{y}}, z_0\hat{\boldsymbol{z}})$, where $\hat{\boldsymbol{x}}$, $\hat{\boldsymbol{y}}$, and $\hat{\boldsymbol{z}}$ are the unit vectors of the *x*-axis, *y*-axis, and *z*-axis, respectively. The dipole axis points toward $\hat{\boldsymbol{M}}\,(\sin\theta_0\cos\varphi_0\hat{\boldsymbol{x}}, \sin\theta_0\sin\varphi_0\hat{\boldsymbol{y}}, \cos\theta_0\hat{\boldsymbol{z}})$, where $\hat{\boldsymbol{M}}$ is the unit direction of dipole moment $\boldsymbol{M}$, and $\theta_0(0° \leqslant \theta_0 \leqslant 180°)$ and $\varphi_0(0° \leqslant \varphi_0 \leqslant 360°)$ are the polar angle and azimuthal angle of $\hat{\boldsymbol{M}}$, respectively. At time t_i, the spacecraft is located at $\boldsymbol{r}_i\,(x_i\hat{\boldsymbol{x}}, y_i\hat{\boldsymbol{y}}, z_i\hat{\boldsymbol{z}})$, and the recorded magnetic field vector is $\boldsymbol{B}_i$. The position vector of the spacecraft relative to the dipole center is $\boldsymbol{R}_i = \boldsymbol{r}_i - \boldsymbol{r}_0$. During the period of measurement, $\hat{\boldsymbol{M}}$ is assumed to be fixed. In this study, we aim to invert the dipole parameters by using the sampled magnetic vectors $\boldsymbol{B}_i$ along the trajectory and $\boldsymbol{r}_i$ by the spacecraft.

It is convenient to construct a planetocentric dipole coordinate, which is defined as

$$\begin{cases} \hat{\boldsymbol{z}}' = \hat{\boldsymbol{M}}, \\ \hat{\boldsymbol{y}}' = \dfrac{\hat{\boldsymbol{z}}' \times \hat{\boldsymbol{x}}}{|\hat{\boldsymbol{z}}' \times \hat{\boldsymbol{x}}|}, \\ \hat{\boldsymbol{x}}' = \hat{\boldsymbol{y}}' \times \hat{\boldsymbol{z}}', \end{cases} \tag{1}$$

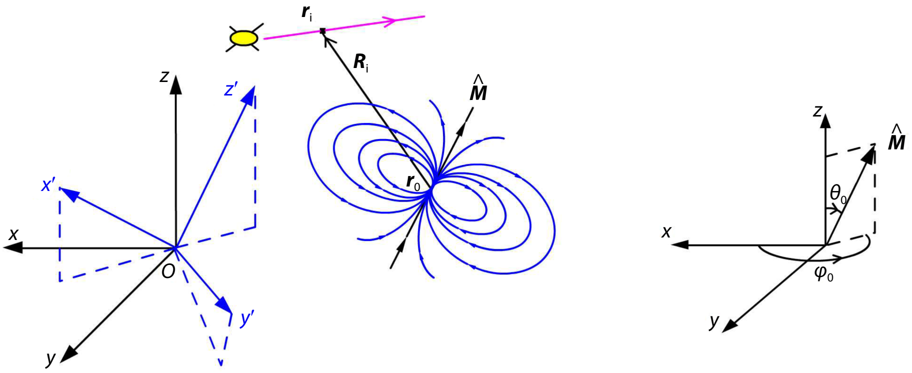

Figure 1. The location of a magnetic dipole in a planetocentric coordinate xyz that corotates with the planet. The dipole is located at point $\boldsymbol{r}_0$ with the axial orientation along $\hat{\boldsymbol{M}}$, which is determined by its polar angle θ_0 and azimuthal angle φ_0 in the planetocentric coordinate. In the frame of xyz, we can set up a dipole coordinate $x'y'z'$ (see the details in the text). Note that the origin of the dipole coordinate is at point O (center of the planet). The magenta line labels the trajectory of the spacecraft. At the moment of t_i, the spacecraft makes a magnetic field measurement at location $\boldsymbol{r}_i$, whose relative position vector to the dipole center is $\boldsymbol{R}_i$.

with its origin being point O (center of the planet) and with the dipole center $\boldsymbol{r}_0$ at $\left(x_0'\hat{\boldsymbol{x}}', y_0'\hat{\boldsymbol{y}}', z_0'\hat{\boldsymbol{z}}'\right)$ in the dipole coordinates. If the origin point is placed at the dipole center, the dipole coordinate can be modified to be dipole centered. Note that unless stated otherwise, the superscript prime symbol means the vector is expressed in the planetocentric dipole coordinate.

2.2 The Dipole Axis and the Transverse Offset of the Dipole Center

Because the ideal dipole field has no azimuthal component, the field lines, diverged from or converged into the dipole center, should be radially oriented in the equatorial plane of the dipole coordinates. Therefore, the dipole axis should be the orientation along which the projected field lines are best radially oriented. Following the method of Rong ZJ et al. (2021), we can find the optimal dipole axis, $\hat{\boldsymbol{M}}$, and the transverse offset of the dipole center, x_0' and y_0', in the equatorial plane of the dipole coordinate. In addition, the dipole axis error yielded can be indicated by a dimensionless parameter, α_min. Readers can refer to the detailed algorithm in Section 2.1 of Rong ZJ et al. (2021).

2.3 The Axial Shift of the Dipole Center

Once the optimal axial orientation and the transverse shift of the dipole center are found, we can similarly follow the method of Rong ZJ et al. (2021) to determine the shift of the dipole center along the axis. The only difference is that we have to deal with the analytic formula of the ideal dipole model instead of the loop model. The detailed procedures are as follows.

Given an ideal dipole field, $\boldsymbol{B}_0$, measured by a spacecraft, the Cartesian components of the dipole field measured by the spacecraft at the moment of t_i can be written as

$$\begin{cases} \tilde{B}_{0ix} = \dfrac{3\mu_0 M\tilde{x}_i\tilde{z}_i}{4\pi R_i^5}, \\ \tilde{B}_{0iy} = \dfrac{3\mu_0 M\tilde{y}_i\tilde{z}_i}{4\pi R_i^5}, \\ \tilde{B}_{0iz} = -\dfrac{\mu_0 M\left(R_i^2 - 3\tilde{z}_i^2\right)}{4\pi R_i^5}, \end{cases} \tag{2}$$

where R_i is the radial distance of the spacecraft to the dipole center and M is the dipole strength. The overhead tilde means that the field components are expressed in dipole-centered coordinates (because it is within the frame defined in Equation (1), but with the origin shifted to the dipole center).

Thus, as shown in Figure 1, the radial distance, R_i, is

$$R_i = |\boldsymbol{r}_i - \boldsymbol{r}_0| = \sqrt{\tilde{x}_i^2 + \tilde{y}_i^2 + \tilde{z}_i^2} = \sqrt{\left(x_i' - x_0'\right)^2 + \left(y_i' - y_0'\right)^2 + \left(z_i' - z_0'\right)^2}, \tag{3}$$

where x_i', y_i', and z_i' are the three Cartesian components of $\boldsymbol{r}_i$ in the dipole coordinates, and x_0', y_0', and z_0' are the three Cartesian components of the dipole center, $\boldsymbol{r}_0$, in the dipole coordinates.

Because the parameters $\hat{\boldsymbol{M}}$, x_0', and y_0' have been derived in Subsection 2.2, the components $\tilde{B}_{0ix}$, $\tilde{B}_{0iy}$, and $\tilde{B}_{0iz}$ actually become the functions of M and z_0'. Considering that the field configuration of the ideal dipole field is independent of the moment strength, the orientation of unit field vectors,

$$\tilde{\boldsymbol{b}}_{0i} = \frac{\tilde{B}_{0ix}}{B_{0i}}\hat{\boldsymbol{x}}' + \frac{\tilde{B}_{0iy}}{B_{0i}}\hat{\boldsymbol{y}}' + \frac{\tilde{B}_{0iz}}{B_{0i}}\hat{\boldsymbol{M}}, \tag{4}$$

where $B_{0i} = \sqrt{\tilde{B}_{0ix}^2 + \tilde{B}_{0iy}^2 + \tilde{B}_{0iz}^2} = \dfrac{\mu_0 M}{4\pi R_i^3}\sqrt{1 + 3\left(\dfrac{\tilde{z}_i}{R_i}\right)^2}$, is determined only by z_0'.

In contrast, the unit field vector actually recorded is $\boldsymbol{b}_i = \dfrac{\boldsymbol{B}_i}{|\boldsymbol{B}_i|}$; thus, the optimal axial shift of the dipole center, z_0', should make $\tilde{\boldsymbol{b}}_{0i}$ best parallel to $\boldsymbol{b}_i$. As such, the angle between $\boldsymbol{b}_i$ and $\tilde{\boldsymbol{b}}_{0i}$ (which we defined as γ_i) is a function of z_0', that is,

$$\gamma_i = \mathrm{acos}\left(\boldsymbol{b}_i \cdot \tilde{\boldsymbol{b}}_{0i}\right). \tag{5}$$

Thus, one can construct a residue function as

$$\varepsilon\left(z_0'\right) = \frac{1}{N}\sum\nolimits_i \gamma_i. \tag{6}$$

Obviously, ε is a function of z_0'. The optimal z_0' should make ε reach a global minimum. Thus, one can search for the minimum of ε quickly to find the corresponding optimal value of z_0'.

One can adopt an alternative way of inferring the optimal z_0' if one notices that the location of the magnetic equator plane (the radial component of the field in cylindrical coordinates equals zero) is determined by the axial shift of the dipole center. In other words, the axial shift of the dipole center can alternatively be identified according to the location of the reversal of the recorded series of radial components in the dipole-centered cylindrical coordinates. Anderson et al. (2011) adopted this method previously in determining the northward shift of Mercury's dipole center. However, to guarantee the accuracy of the identified axial shift in this way, a higher sampling rate is required when spacecraft are crossing the magnetic equatorial plane. Moreover, the external field is required to be negligible near the magnetic equatorial plane. These requirements are not always well-satisfied. Thus, to address the sampled dataset in general, we would rather use Equation (6) to derive the optimal axial shift in the present study.

2.4 The Dipole Moment

Because the optimal axis orientation and the dipole center have been derived in the preceding subsections, we can continue with the method of Rong ZJ et al. (2021) to infer the strength of the dipole moment. Specifically, we can construct a least-squares error,

$$\delta=\frac{1}{N}\sum_i\frac{|\boldsymbol{B}_{i0}-\boldsymbol{B}_i|}{|\boldsymbol{B}_{i0}|},\tag{7}$$

to evaluate how much the recorded field, $\boldsymbol{B}_i$, deviates from the fitted dipole field, $\boldsymbol{B}_{i0}$. Note that Rong ZJ et al. (2021) took the denominator as $|\boldsymbol{B}_i|$ (see their Equation (17)), but here we correct it as $|\boldsymbol{B}_{i0}|$ by analogy with the formula for the relative standard deviation. Because the optimal axis orientation and the dipole center have been derived, δ consequently becomes a function of the strength of the dipole moment, M, and the optimal M can be searched when the δ reaches a minimum.

2.5 Summary of the Technique

In stark contrast to the previous traditional least-squares methods with all parameters fitted simultaneously, our technique can separate the dipole parameters and successively invert these parameters:

(1) We can first determine the dipole axis and the transverse offset of the dipole center according to the projection of measured magnetic field directions.

(2) We can proceed to determine the axial shift of the dipole center by matching the field directions with the ideal dipole field directions.

(3) Finally, on the basis of these derived parameters, we can derive the optimal dipole moment when the field strength is considered.

The algorithm test and theoretical proof of this inversion technique are very similar to those of the loop model, which is given in the Supporting Information of Rong ZJ et al. (2021). The algorithm test demonstrates that our technique can invert the dipole parameters exactly if the sampled field vectors are from the ideal dipole field (not shown here). Thus, the inversion errors of $\alpha_{\min}$, ε, and δ are usually generated by a disturbance of the external field or the nondipole field components. In the following section, we show how this inversion algorithm is applied to the sampled dataset of the magnetic field.

3. Applications

3.1 Application to the IGRF Field

To demonstrate the ability of this technique, we apply it to the 13th-generation IGRF model (Alken et al., 2021) to infer the dipole source of the geomagnetic field. Because the IGRF model describes the large-scale internal field of the geomagnetic field, our technique based on the sampled data points from the IGRF will yield a dipole model that best fits the sampled dataset of the 13th IGRF model.

As shown in Figure 2, we arbitrarily construct four synthetic polar circular orbits at an altitude of 500 km (inclinations of all orbits are set at 90°), which homogeneously cover the longitude with a longitude step of 45° in geocentric coordinates. The spacecraft evenly samples 20 data points along each orbit. In total, 80 data points are obtained from the four orbits. Note that in the calculation of the IGRF field, all the Gauss coefficients of the 13th IGRF model are used, the mean earth radius is set as 6371.2 km, and the time of 2020-01-01 00:00:00 is arbitrarily set.

Figure 3a shows the series of 80 sampled magnetic field vectors in the geocentric coordinates. With the sampled dataset, we calculated the angular errors, $\alpha_{\min}$, of all possible axial orientations, $\hat{\boldsymbol{M}}(\theta_0,\varphi_0)$. The $\alpha_{\min}$ is an error indicator describing how much the magnetic vectors projected along the candidate axis deviated from the radial direction. One can refer to Equation (3) of Rong ZJ et al. (2021) to find the specific definition of $\alpha_{\min}$. The optimum of

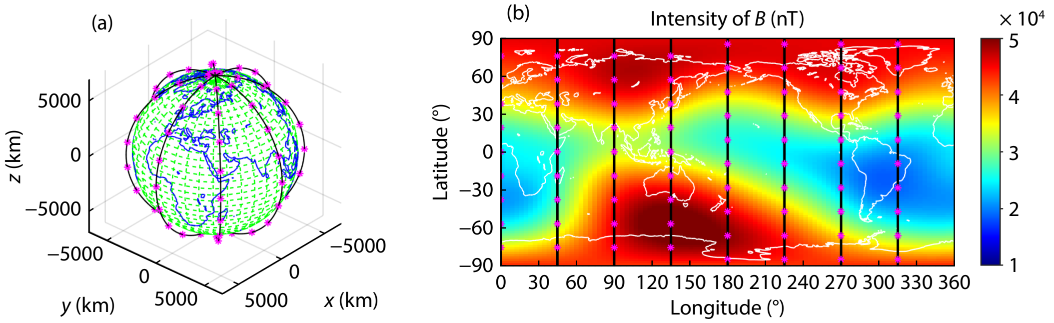

Figure 2. (a) The four virtual spacecraft orbits (black circles) and the locations when sampling the magnetic field (magenta stars) in the geocentric coordinates. (b) Global maps of the magnetic field intensity from the 13th IGRF model (the time used to calculate the model was arbitrarily set as 2020-01-01 00:00:00) at an altitude of 500 km, overlapping the projected trajectories of the four orbits.

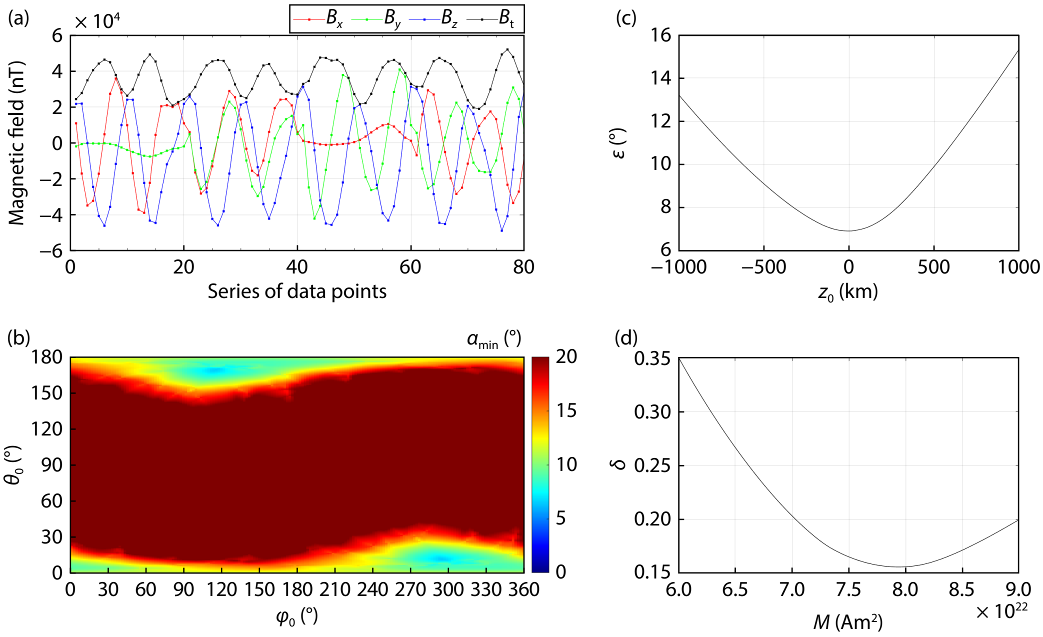

Figure 3. Scheme of the inversion procedures. (a) The series of sampled data points of the IGRF field at an altitude of 500 km. (b) The distribution of $\alpha_{\min}$. (c) The variation of ε against z'_0. (d) The variation of δ against M.

$\hat{\boldsymbol{M}}(\theta_0, \varphi_0)$ has a corresponding global minimum of $\alpha_{\min}$.

Figure 3b shows the two-dimensional (2D) distribution of $\alpha_{\min}$ on a map constituted by the polar angle θ_0 and azimuthal angle φ_0 of the candidate axial orientations. As expected, two local minima of $\alpha_{\min}$ are present in Figure 3b because the two minima correspond to the parallel and antiparallel directions of the optimal $\hat{\boldsymbol{M}}$. We choose the one that points nearly toward the southern pole as the optimal direction of $\hat{\boldsymbol{M}}$. Thus, the final optimal $\hat{\boldsymbol{M}}$ is found as ($\theta_{0m} = 168.7°, \varphi_{0m} = 114.3°$), and, accordingly, the optimal transverse offset of the dipole center in the dipole coordinate is calculated as ($x'_{0m} = -299$ km, $y'_{0m} = -355$ km).

After the derivation of $\hat{\boldsymbol{M}}$, x'_{0m}, and y'_{0m}, the optimal axial shift of the dipole center in the dipole coordinate is found to be $z'_{0m} = 0$ km when the residue error ε defined in Equation (6) reaches a minimum (Figure 3c). Finally, given the derived $\hat{\boldsymbol{M}}$, x'_{0m}, y'_{0m}, and z'_{0m}, the optimal dipole moment is calculated as $M_m = 7.94 \times 10^{22}$ Am^2 when the least-squares error δ defined in Equation (7) reaches a minimum (Figure 3d).

By applying Equation (1), the transformation of the dipole center $\boldsymbol{r}_0\left(x'_{0m} = -299, y'_{0m} = -355, z'_{0m} = 0\right)$ km from the dipole coordinate to the geocentric coordinate yields $\boldsymbol{r}_0$ ($x_{0m} = -298, y_{0m} = 345$, $z_{0m} = 87$) km.

We can calculate the inverted dipole field based on these inverted dipole parameters. As shown in Figure 4, the inverted dipole

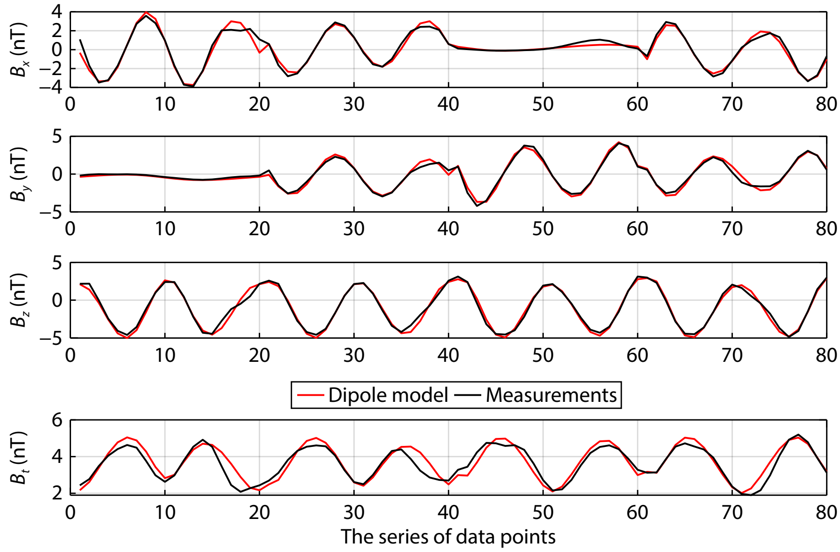

Figure 4. Comparison showing a sampled IGRF field (black lines) and the magnetic field from the inverted dipole (red lines). Panels from top to bottom show the three components of the magnetic field in the geocentric coordinate and the field strength, respectively.

model agrees well with the sampled IGRF field, suggesting that the inverted dipole parameters are reasonable.

If we lift the four orbits to a higher altitude, the same inversion scheme will yield an inverted dipole with lower errors. Table 1 tabulates the fitted parameters and the associated errors when the spacecraft is at different altitudes. It is clear that as the orbit altitudes increase, the fitted parameters approach the values of an eccentric dipole model (Fraser-Smith, 1987) with decreasing errors. The better fit to the dipole field with the increase in altitude is reasonable because the field contributions from the higher orders will attenuate with altitude more quickly than those of the dipole field. Table 1 compares the parameters of the traditional eccentric dipole model and its relative standard deviation corresponding to the sampled dataset at different altitudes.

Moreover, it is expected that if the orbits could cover the longitude more intensively, the inverted parameters would be less affected by the bias of magnetic anomalies in longitude. Given a fixed altitude of 500 km, Table 2 shows the inverted results when more orbits distributed evenly in longitude are involved. If only one orbit plane is considered (e.g., the second row of Table 2), the inversion error δ is more significant, and as the orbit number increases, the inverted parameters and the associated errors (decreased with orbit number) approach stability. Indeed, the sampled data points at an altitude of 500 km are still significantly affected by the magnetic anomalies, such as the South Atlantic Anomaly (Amit et al., 2021; Yue YC et al., 2024); thus, as indicated by the errors, the inverted parameters have a modest departure from the ideal dipole model, even though more orbits are involved.

3.2 Application to the Martian Crustal Field

Our inversion technique could help diagnose the interior source of a local magnetic anomaly. To demonstrate the ability of this technique, we also apply it to study the local source of the Martian crustal field within selected local regions.

The state-of-the-art Martian crustal field model with a spherical harmonic degree of 110 developed by Gao JW et al. (2021) is used here (referred to hereafter as G110). In comparison with many other models developed earlier (e.g., Cain et al., 2003; Morschhauser et al., 2014; Langlais et al., 2019), the G110 can better describe the distribution of the crustal field above an altitude of 120 km.

The pattern of the Martian crustal field patches (see left panel of Figure 5) demonstrates that the interior magnetic sources are distributed irregularly. Estimating the depths of the magnetization source is a challenge (Mittelholz and Johnson, 2022), although

Table 1. The inverted dipole parameters for the sampled dataset of the IGRF-13 field at different altitudes when the time is set at 2020-01-01 00:00:00.

Altitude (km)	x_{0m} (km)	y_{0m} (km)	z_{0m} (km)	M (10^{22} Am^2)	θ_{0m} (°)	φ_{0m} (°)	$\alpha_{\min}$ (°)	ε (°)	δ	δ_1 [a]
0	−274	336	85	8.04	168.1	116.6	7.4	8.1	0.182	0.192
500	−298	345	87	7.94	168.7	114.3	6.5	6.9	0.156	0.164
1500	−327	359	108	7.84	170.1	112.6	5.3	5.3	0.119	0.125
3000	−350	366	159	7.78	171.2	111.5	4.3	4.0	0.089	0.091
5000	−365	369	205	7.74	171.7	110.5	3.5	3.1	0.067	0.066
10,000	−382	372	234	7.71	171.4	108.6	2.2	1.9	0.040	0.038
50,000	−395	376	225	7.71	170.7	107.2	0.6	0.5	0.009	0.009

[a] The traditional eccentric dipole model is shown for comparison, whose displacement of the dipole center is calculated by using only the first eight internal Gauss coefficients (see Equations (16)–(18) in Fraser-Smith, 1987) (The derived displacement of the eccentric dipole is (x_{0m} = −398, y_{0m} = 372, z_{0m} = 227) km, the dipole moment is $M = 7.71\cdot10^{22}$ Am^2, and the dipole orientation is (θ_{0m} = 170.6°, φ_{0m} = 107.3°).). Note that the direction of the dipole axis of the eccentric dipole is set to be the same as that of the geocentric dipole. Inversion error δ_1 is the relative standard deviation of the eccentric dipole model, which is calculated using Equation (7).

Table 2. The inverted dipole parameters for the sampled datasets of the IGRF-13 field when different orbit numbers are considered.

Longitude step[a] (°)	x_{0m} (km)	y_{0m} (km)	z_{0m} (km)	M (10^{22} Am^2)	θ_{0m} (°)	φ_{0m} (°)	$\alpha_{\min}$ (°)	ε (°)	δ
180	−257	327	365	7.72	171.2	109.8	3.8	7.7	0.217
90	−431	366	11	7.88	170.1	117.7	3.8	6.9	0.174
45	−298	345	87	7.94	168.7	114.3	6.5	6.9	0.156
30	−304	355	73	7.93	169.6	116.3	6.2	6.7	0.153
10	−303	357	71	7.93	169.6	116.4	6.7	6.6	0.151
5	−301	351	86	7.91	168.4	115.2	6.8	6.8	0.154
2	−301	352	84	7.91	168.4	115.4	6.8	6.8	0.154

[a] The angle between neighboring orbit planes. In other words, the orbit number equals 180/step.

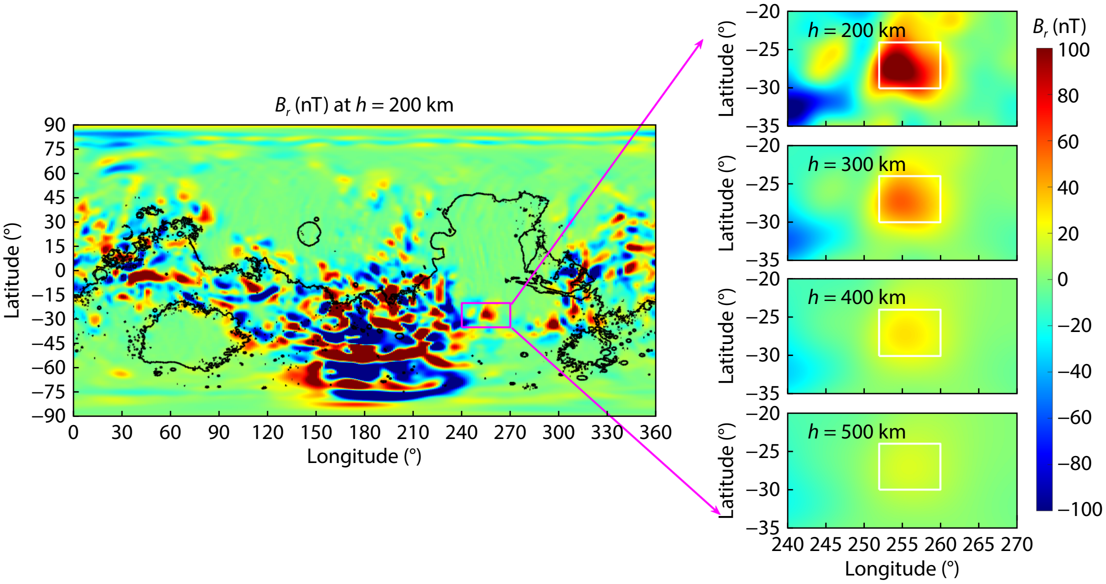

Figure 5. The left panel shows the distribution map of the radial component (B_r) of the Martian crustal field at an altitude (h) of 200 km in planetocentric coordinates (the black curves represent the reference of altitude being zero from the Mars Orbiter Laser Altimeter dataset; Neumann et al., 2001). The right panels, from top to bottom, show the zoomed-in maps of Region 1 at altitudes of 200, 300, 400, and 500 km, respectively. Mars' radius is set as 3390 km.

some statistical studies have been conducted based on the fitting of a theoretical power spectrum to the magnetic field models (e.g., Voorhies, 2008; Lewis and Simons, 2012; Gong SX and Wieczorek, 2021). A single dipole model cannot describe the entire distribution of the crustal field. However, in some local regions, the local field might fit the dipole field, and our technique might work to diagnose the local magnetic source. To avoid interference from the neighboring patches of the crustal field, we arbitrarily select two field patches that appear isolated to test our technique. The selected Region 1 covers the latitude of approximately −30° to −24° and longitude of approximately 252° to 260° (see the white rectangles in the right panels of Figure 5), and the selected Region 2 covers the latitude of approximately −37° to −30° and longitude of approximately 292° to 299° (see the white rectangles in the right panels of Figure 6). The field radial component peaks in these local regions; thus, these regions are presumed to be closer to the pole of the local anomaly, and the field should be less affected by interference from the neighboring field patches.

3.2.1 *Application to Region 1*

In the selected Region 1, which covers a latitude of approximately −30° to −24° and a longitude of approximately 252° to 260°, we evenly sample the G110 field 30 times latitudinally and 30 times

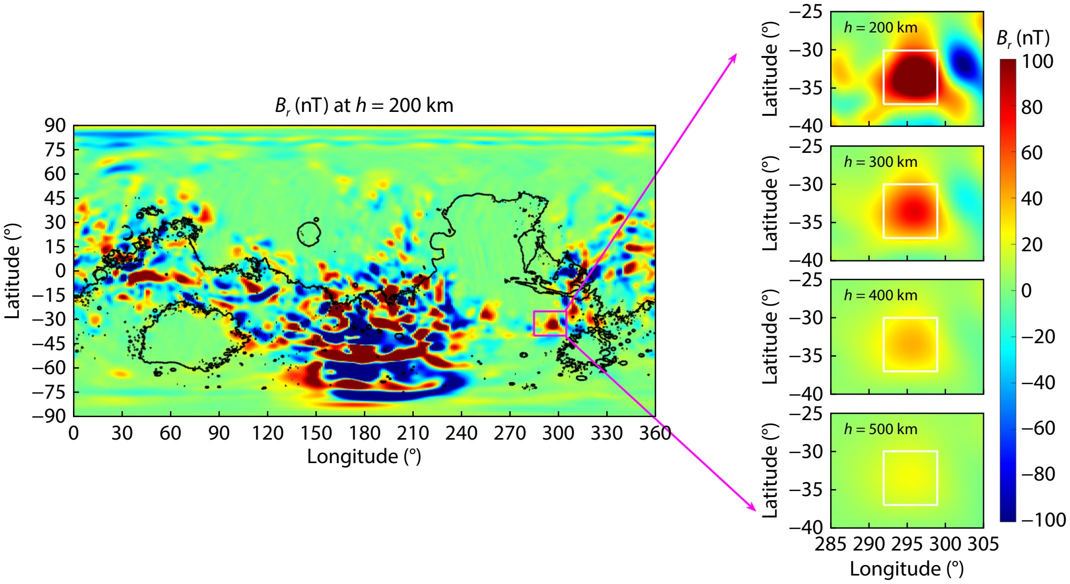

Figure 6. The crustal field distribution over Region 2. The format is the same as that of Figure 5.

longitudinally. Thus, we sample 900 data points in total (30 points in latitude × 30 points in longitude) at a fixed altitude.

We apply the same technique to the sampled datasets at altitudes of 200, 300, 400, and 500 km, respectively. Table 3 summarizes the optimal dipole parameters and the associated errors derived.

The error indicators in Table 3 demonstrate that the sampled field datasets are closer to a dipole field with an increase in altitude. At altitudes higher than 400 km, the sampled field can be approximated well by a dipole whose depth is ~90–100 km and the moment strength is ~$2.8–2.9 \times 10^{16}$ Am^2. In contrast, at altitudes lower than 300 km, the sampled field dataset gradually departs from the dipole field. Notably, at an altitude of 200 km, the inverted dipole center is unreasonably located above the Martian surface. The reason may be that many fine patches of the crustal field would appear at lower altitudes, which would make the fitting depart substantially from the dipole field at lower altitudes.

3.2.2 Application to Region 2

In the selected Region 2, which covers a latitude of approximately −37° to −30° and a longitude of approximately 292° to 299°, we similarly evenly sample 900 data points (30 points in latitude × 30 points in longitude) at a fixed altitude (Figure 6). We again apply the same technique to the sampled datasets at altitudes of 200, 300, 400, and 500 km, respectively. The optimal dipole parameters and the associated errors derived are summarized in Table 4.

As indicated by the significant fitting errors, it is clear that the crustal fields in Region 2 cannot be approximated well by a dipole model. Although the sampled field is closer to a dipole field at a higher altitude, as indicated by the modestly reduced errors with the increase in altitude, the inverted dipole center is nonetheless unreasonably located above the planetary surface. The interference of the ambient crustal fields might account for the unreasonable inverted dipole center.

Therefore, on the basis of the applications above to the two regions of local field anomalies, several caveats to the dipole inversion of the local anomaly can be obtained:

(1) The crustal field is closer to the dipole field at a higher altitude. However, because of the interference of the ambient field, the dipole inversion at higher altitudes may result in unreasonable inversion parameters.

(2) The locations of the sampled field dataset at lower altitudes are closer to the magnetic sources. Nonetheless, many fine patches of crustal field magnetic sources could appear at lower altitudes, and the interference of the fields of these patches at lower altitudes could distort the field structure from the dipole field.

(3) Because our technique fits the sampled data points best by the dipole field, the inversion results are strongly dependent on the area of the sampled dataset. The test showed that the area of sampled regions, although around the peak of the anomaly, could affect the final inversion results (not shown here). The smaller area centered by the peak field strength of the local anomaly, although it could decrease the interference of ambient patches of the crustal field, would result in a set of unreasonable fitted parameters. In contrast, the sampled dataset of a larger area, although it could yield more reasonable parameters in terms of larger scale fitting, would inevitably include more interference of the ambient fields.

Overall, our dipole inversion technique can diagnose the interior source of a local magnetic anomaly, but caution is needed when applying it. To determine the inverted parameters consistently and reasonably, one should check the different altitudes and areas of the sampled dataset.

4. Discussion

We must keep in mind that our technique relies on three error

Table 3. The inverted dipole parameters for Region 1 at different altitudes.

Altitude (km)	x_{0m} (km)	y_{0m} (km)	z_{0m} (km)	H[a] (km)	M (10^{16} Am^2)	θ_{0m} (°)	φ_{0m} (°)	$\alpha_{\min}$ (°)	ε (°)	δ
200	−962	−2886	−1478	−8	2.83	107	356	3.0	10.6	0.386
300	−939	−2834	−1471	62	2.85	107	337	2.0	4.3	0.157
400	−906	−2820	−1456	90	2.88	111	327	1.4	2.0	0.060
500	−879	−2824	−1444	99	2.81	114	322	0.9	1.4	0.038

[a] H is the depth of the inverted dipole center, which equals the value of the Mars radius (3390 km) minus the radial distance of the dipole center.

Table 4. The inverted dipole parameters for Region 2.

Altitude (km)	x_{0m} (km)	y_{0m} (km)	z_{0m} (km)	H[a] (km)	M (10^{16} Am^2)	θ_{0m} (°)	φ_{0m} (°)	α_{min} (°)	ε (°)	δ
200	1174	−2446	−1991	25	2.87	57	298	4.6	13.7	0.409
300	1164	−2456	−2002	14	2.35	62	297	2.8	9.7	0.283
400	1163	−2475	−2057	−32	2.08	54	296	1.9	9.1	0.262
500	1192	−2483	−2131	−93	1.95	44	288	1.0	9.0	0.270

[a] The format is the same as that of Table 3.

proxies—namely, $\alpha_{\min}$ for the orientation error of the dipole axis, ε for the error of the dipole center along the axis, and δ for the error of the dipole moment—to comprehensively evaluate the inversion quality. Thus, in terms of our optimal criterion, relying only on the least-squares error δ, one criterion is far from enough to determine the inversion quality. In other words, different sets of dipole parameters would probably yield the same δ. Therefore, the less δ yielded by the other inversion methods or models does not necessarily imply that the quality of their derived parameters is better than what we derived from our methods (see Table 1).

We have made a comparison with the loop model developed previously by Rong ZJ et al. (2021; see Table S1 in Supplementary Material). The comparison suggests that the inverted parameters for both models are nearly the same; thus, the reduced dipole model is sufficient to describe the dipolarity of the geomagnetic field. However, the inversion of the seven parameters of a loop model shows a minor improvement (smaller δ) in the model fitting relative to the six parameters of the dipole model. This minor improvement is to be expected because a model with more parameters can depict the field more accurately. In future studies, one could consider other complicated models, such as a cylindrical current model or a spherical current model.

Apart from the main dipole component, the real geomagnetic field also includes some large-scale geomagnetic anomalies, such as the Southern Atlantic Anomaly. Thus, to describe the geomagnetic field better, previous studies have presented some models of multiple dipoles (e.g., Alldredge and Hurwitz, 1964; Alldredge and Stearns, 1969; Mayhew and Estes, 1983); again, a least-squares procedure with the fitting of multiple parameters was involved in these studies, and the problem of multiple local solutions cannot be avoided. We could further develop a new multiple-dipole model of the geomagnetic field based on our dipole technique. If we were to subtract the inverted dipole model from the IGRF field, the remnant field could highlight the distribution of geomagnetic anomalies. The performance of this technique around each anomaly would derive the dipole source of the corresponding anomaly. A detailed algorithm for the multiple-dipole model will be presented in a later study. We must emphasize that this technique can not only complement the traditional SHA of geomagnetic fields but can also be used as an independent method of diagnosing the planetary dipolar field when SHA fails.

5. Conclusions

As a continuation of the technique by Rong ZJ et al. (2021), we developed an inversion technique based on a dipole model to invert the magnetic source of the dipolar magnetic field. On the basis of the sampled dataset of magnetic vectors, this technique is able to separate and invert the dipole parameters successively, which can effectively avoid the traditional dilemma of local solutions when fitting all the parameters simultaneously. The application of this technique to the IGRF model of the geomagnetic field demonstrates its reasonableness and applicability. The applications to the Martian crustal field model demonstrate that this technique can also be used to invert the magnetic source of the local magnetic anomaly but that the validity of the inversion should be interpreted with caution.

Acknowledgments

This work is supported by the National Natural Science Foundation of China (Grant No. 42388101), the Key Research Program of the Chinese Academy of Sciences (Grant No. ZDBS-SSW-TLC00103), and the Key Research Program of the Institute of Geology and Geophysics, Chinese Academy of Sciences (IGGCAS-202102).

Competing Interests

The authors have no conflicts of interest to declare.

Open Research

The Supporting Information includes Table S1 in Supplementary Material. The Gauss coefficients of the IGRF model used in this paper are available from Alken et al. (2021). The Gauss coefficients of the G110 model of the Martian crustal field are available from Gao JW et al. (2021).

Data Availability Statement

The package of Matlab codes involved in this study is archived at Zenodo and is publicly accessible via https://zenodo.org/doi/10.5281/zenodo.13777127

References

Alken, P., Thébault, E., Beggan, C. D., Amit, H., Aubert, J., Baerenzung, J., Bondar, T. N., Brown, W. J., Califf, S., … Zhou, B. (2021). International Geomagnetic Reference Field: The thirteenth generation. *Earth Planets Space*, *73*, 49. https://doi.org/10.1186/s40623-020-01288-x

Alldredge, L. R., and Hurwitz, L. (1964). Radial dipoles as the sources of the Earth's main magnetic field. *J. Geophys. Res.*, *69*(12), 2631–2640. https://doi.org/10.1029/JZ069i012p02631

Alldredge, L. R., and Stearns, C. O. (1969). Dipole model of the sources of the Earth's magnetic field and secular change. *J. Geophys. Res.*, *74*(27), 6583–6593. https://doi.org/10.1029/JB074i027p06583

Amit, H., Terra-Nova, F., Lézin, M., and Trindade, R. I. (2021). Non-monotonic growth and motion of the South Atlantic anomaly. *Earth Planets Space*, *73*(1), 38. https://doi.org/10.1186/s40623-021-01356-w

Anderson, B. J., Johnson, C. L., Korth, H., Purucker, M. E., Winslow, R. M., Slavin, J. A., Solomon, S. C., McNutt, R. L., Raines, J. M., and Zurbuchen, T. H. (2011). The global magnetic field of Mercury from MESSENGER orbital observations. *Science*, *333*(6051), 1859–1862. https://doi.org/10.1126/science.1211001

Cain, J. C., Ferguson, B. B., and Mozzoni, D. (2003). An $n = 90$ internal potential function of the Martian crustal magnetic field. *J. Geophys. Res.: Planets*, *108*(E2), 5008. https://doi.org/10.1029/2000JE001487

Chapman, S., and Bartels, J. (1940). *Geomagnetism*. Oxford, UK: Oxford University Press.

Demina, I. M., and Farafonova, Y G. (2016). Inverse problem for the current loop model: Possibilities and restrictions. *Geomagn. Aeron.*, *56*(4), 415–425. https://doi.org/10.1134/s0016793216030038

Fraser-Smith, A. C. (1987). Centered and eccentric geomagnetic dipoles and their poles, 1600–1985. *Rev. Geophys.*, *25*(1), 1–16. https://doi.org/10.1029/RG025i001p00001

Gao, J. W., Rong, Z. J., Klinger, L., Li, X. Z., Liu, D., and Wei, Y. (2021). A spherical harmonic Martian crustal magnetic field model combining data sets of MAVEN and MGS. *Earth Space Sci.*, *8*(10), e2021EA001860. https://doi.org/10.1029/2021EA001860

Gong, S. X., and Wieczorek, M. (2021). Depth of Martian magnetization from localized power spectrum analysis. *J. Geophys. Res.: Planets*, *126*(8), e2020JE006690. https://doi.org/10.1029/2020JE006690

Langlais, B., Thébault, E., Houliez, A., Purucker, M. E., and Lillis, R. J. (2019). A new model of the crustal magnetic field of Mars using MGS and MAVEN. *J.*

Geophys. Res.: Planets, *124*(6), 1542–1569. https://doi.org/10.1029/2018JE005854

Lewis, K. W., and Simons, F. J. (2012). Local spectral variability and the origin of the Martian crustal magnetic field. *Geophys. Res. Lett.*, *39*(18), L18201. https://doi.org/10.1029/2012GL052708

Mayhew, M. A., and Estes, R. H. (1983). Equivalent source modeling of the core magnetic field using Magsat data. *J. Geomagn. Geoelectr.*, *35*(4), 119–130. https://doi.org/10.5636/jgg.35.119

Merrill, R. T., McElhinny, M. W., and McFadden, P. L. (1996). *The Magnetic Field of the Earth: Paleomagnetism, the Core, and the Deep Mantle* (2nd ed., pp. 17–46). San Diego, CA: Academic Press.

Mittelholz, A., and Johnson, C. L. (2022). The Martian crustal magnetic field. *Front. Astron. Space Sci.*, *9*, 895362. https://doi.org/10.3389/fspas.2022.895362

Morschhauser, A., Lesur, V., and Grott, M. (2014). A spherical harmonic model of the lithospheric magnetic field of Mars. *J. Geophys. Res.: Planets*, *119*(6), 1162–1188. https://doi.org/10.1002/2013JE004555

Ness, N. F., Behannon, K. W., Lepping, R. P., Whang, Y. C., and Schatten, K. H. (1974). Magnetic field observations near Mercury: Preliminary results from Mariner 10. *Science, 185*(4146), 151–160. https://doi.org/10.1126/science.185.4146.151

Neumann, G. A., Rowlands, D. D., Lemoine, F. G., Smith, D. E., and Zuber, M. T. (2001). Crossover analysis of Mars Orbiter Laser Altimeter data. *J. Geophys. Res.: Planets*, *106*(E10), 23753–23768. https://doi.org/10.1029/2000JE001381

Peddie, N. W. (1979). Current loop models of the Earth's magnetic field. *J. Geophys. Res.: Solid Earth*, *84*(B9), 4517–4523. https://doi.org/10.1029/JB084iB09p04517

Rong, Z. J., Wei, Y., Klinger, L., Yamauchi, M., Xu, W. Y., Kong, D. L., Cui, J., Shen, C., Yang, Y. Y., … Chai, L. H. (2021). A new technique to diagnose the geomagnetic field based on a single circular current loop model. *J. Geophys. Res.: Solid Earth*, *126*(11), e2021JB022778. https://doi.org/10.1029/2021JB022778

Sano, Y. (1991). A best-fit eccentric dipole and the invariance of the Earth's dipole moment. *J. Geomagn. Geoelectr.*, *43*(10), 825–837. https://doi.org/10.5636/jgg.43.825

Sano, Y., and Sugiura, M. (1992). New definitions of an eccentric dipole for the geomagnetic field. *Phys. Earth Planet. Inter.*, *71*(3-4), 166–179. https://doi.org/10.1016/0031-9201(92)90074-6

Smith, E. J., Davis, L., Jr., and Jones, D. E. (1976). Jupiter's magnetic field and magnetosphere. In *Jupiter: Studies of the Interior, Atmosphere, Magnetosphere and Satellites* (pp. 788–829). Tucson, AZ: University of Arizona Press.

Voorhies, C. V. (2008). Thickness of the magnetic crust of Mars. *J. Geophys. Res.: Planets*, *113*(E4), E04004. https://doi.org/10.1029/2007JE002928

Yue, Y. C., Gao, J. W., He, F., Wei, Y., Cai, S. H., Wang, H. P., Wang, Y. Q., Rong, Z. J., Yao, Z. H., … Pan, Y. X. (2024). Evolution and disappearance of the paleo-West Pacific anomaly: Implications to the future of South Atlantic anomaly. *Phys. Earth Planet. Inter.*, *353*, 107214. https://doi.org/10.1016/j.pepi.2024.107214